The Impact of the Crystallization Processes on the Structural and Optical Properties of Hybrid Perovskites Films

Giulia Grancini[1], Sergio Marras[2], Mirko Prato[2], Cinzia Giannini[3], Claudio Quarti[5], Filippo De Angelis[5], Michele De Bastiani[1], Giles Eperon[4], Henry Snaith[4], Liberato Manna[2], Annamaria Petrozza[1*]*

[1]Center for Nano Science and Technology @Polimi, Istituto Italiano di Tecnologia, via Giovanni Pascoli 70/3, 20133, Milan, Italy

[2]Department of Nanochemistry, Istituto Italiano di Tecnologia, via Morego, 30, 16163 Genova, Italy

[3]Institute of Crystallography, National Research Council, via Amendola 122/O, Bari 70126 Italy

[4]University of Oxford, Clarendon Laboratory, Parks Road, Oxford, OX1 3PU, United Kingdom

[5] Computational Laboratory for Hybrid/Organic Photovoltaics (CLHYO), CNR-ISTM, I-06123, Perugia, Italy

TOC

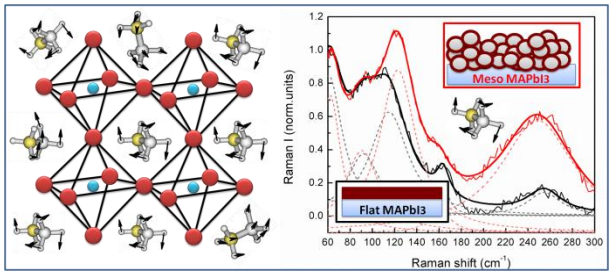

KEYWORDS Perovskite solar cell, Raman spectroscopy, disorder, crystallization, XRD

ABSTRACT. *We investigate the relationship between structural and optical properties of organo-lead mix-halides perovskite films for photovoltaic applications as a function of the crystallization process. The aim is to provide a rational guideline to process perovskite films. For methylammonium lead tri-iodide, we identify a rearrangement of the organic cation in the inorganic cage - random orientation versus hea- to-tail like orientation - moving from smaller crystals grown in a mesoporous scaffold to larger, oriented crystals grown on a flat substrate. This reduces the strain felt by the Pb-I bond featuring the cage and affects the motion of the organic cation in it, consequently affecting the nature of the electronic transition at the onset of the optical absorption spectrum of the semiconductor. We demonstrate that when the PbI_2 precursor is replaced by $PbCl_2$, Pb-I bonds are quickly formed, while Cl species drive the crystallization dynamics before being expelled. In particular they favor the formation of crystals with a preferential order, from a molecular, i.e. organic-inorganic moieties arrangement- to a nano-mesoscopic level, i.e. larger crystals with anisotropic shape. Finally we show that while Cl is mainly expelled from flat films made of large crystals, in presence of an oxide mesoporous scaffold it is partially retained in the composite.*

Since methylammonium lead halide perovskites were identified as promising absorbers for solar cells [1-6] the performance of perovskite-based devices has boosted, reaching power conversion efficiencies as high as 16.7% [7-9]. The perovskite material consists of a MAX_3 structure, where MA sites accommodate the organic cation $(CH_3NH_3)^+$, X the lead halide based on lead cation (Pb^{2+}) and iodine or chlorine (I^-; Cl^-) halide anions. Within this family, the methylammonium lead iodide perovskite ($CH_3NH_3PbI_3$, here on $MAPbI_3$), fabricated from a solution of methylammonium iodide (CH_3NH_3I) and lead iodide (PbI_2), along with its analogous mixed-halide perovskite, known as $CH_3NH_3PbI_{3-x}Cl_x$ and obtained by substituting the PbI_2 precursor with lead chloride ($PbCl_2$), are the two most developed perovskite materials for photovoltaics (PV) [2-4, 10]. Despite the apparently simple and well defined structure based on a tetragonal unit cell made of interconnected PbX_6 octahedra[11], the macroscopic nature, cristallinity and structural organization of the whole perovskite film is still obscure [11-16]. X-ray diffraction (XRD) [11, 13, 17, 18], scanning electron microscopy (SEM) [14] and UV-Vis spectroscopy [19-21], along with electronic structure calculations [22-26] have shown how the perovskite film is intrinsically heterogeneous [12, 27-28], especially in terms of a huge variability in crystal size and aggregation. This was proven to be dependent in particular on the substrate used for film deposition [12, 14, 16, 27]. In the case of $CH_3NH_3PbI_{3-x}Cl_x$ deposited on a flat glass substrate, a polycrystalline film with grain sizes larger than 500 nm is formed, while if the same perovskite is infiltrated into a mesoporous oxide scaffold, the perovskite grains are smaller with an inhomogeneous size distribution ranging from a few nm up to 100 nm [27]. This has a direct impact on the PV parameters, thus the overall solar cell efficiency [12, 27]. Reports on distribution function analysis of XRD patterns [28] on $MAPbI_3$ have recently shown that when integrated into an oxide mesoporous network (either titania [3] or alumina [2]), it

aggregates in a two-phase mixture composed by a 30% of relatively crystalline and ordered component, responsible for the crystalline tetragonal structure observed in the XRD patterns [11, 13, 17, 18], immersed in a mainly disordered nanoscopic-structured matrix characterized by short-range (<2 nm) order [28]. Another hot debate regards the role of chlorine on the crystallization process and how it is affecting the optoelectronic properties of the film [28, 29]. It has been observed that $CH_3NH_3PbI_{3-x}Cl_x$ thin films, for instance, present improved carriers transport properties with respect to $MAPbI_3$ [18, 29], and carriers diffusion length exceeding 1 μm, one order of magnitude larger than that of the $MAPbI_3$, have been demonstrated [30, 31]. It was also shown that increasing the amount of chlorine in the precursor solution of $CH_3NH_3PbI_{3-x}Cl_x$ films leads to an unexpected enhancement of the photoluminescence lifetime [30-32]. It is therefore evident that hybrid perovskites are intrinsically complex materials, in which the presence of various types of interactions and structural disorder play an important role in governing the overall properties. Unfortunately, the currently poor understanding of the relationship between structure and optoelectronic properties prevents the PV community from defining a roadmap for the rational improvement in the photovoltaic performances of such materials and consequently for its technological exploitation [29, 33].

In this work we shine light on the optical and structural properties of both $MAPbI_3$ and $CH_3NH_3PbI_{3-x}Cl_x$ (here on *Cl-doped* $MAPbI_3$) perovskite polycrystalline films. We show that different crystallization processes, i.e. the nature of the substrate and the presence of chlorinated species ($PbCl_2$) in the precursor solution, can affect the interplay between the organic and inorganic moieties and tune the optical band-gap. Moreover, we find that the presence of $PbCl_2$ in the precursors' composition affects the crystal growth process favoring a higher degree of

order from a molecular to a mesoscopic scale, with larger crystals growing with a preferential orientation. Importantly, we prove that chloride ions are released during the growth of large perovskite crystals and no trace of such ions is detected in the final large crystals, while in the presence of a mesoporous metal-oxide scaffold the chloride ions are retained.

As said, $MAPbI_3$ and *Cl-doped* $MAPbI_3$ perovskites have been successfully exploited as active layer either into a mesoporous metal-oxide network or deposited on a flat compact layer [3, 6, 27, 30]. First, we investigate the structure of $MAPbI_3$ by vibrational Raman spectroscopy focusing on the structural properties of a $MAPbI_3$ perovskite film deposited according to established protocols (see Methods in the Supplementary Information) [30, 34] both on a mesoporous scaffold (named "meso" in the following) and on a flat glass surface (named "flat" substrate). Notably, for the "meso" sample, the crystals growth is subject to a constraint, which, on average, reduces the grain size [27]. The vibrational Raman spectrum of the "meso" $MAPbI_3$ (shown in Figure 1) has been previously reported by some of us [34] and the main fingerprint related to both the inorganic (Pb-I stretching and bending modes) and MA cations vibrational modes have been identified [34]. Briefly, the two peaks at lower frequencies, at around 62 cm^{-1} and 94 cm^{-1}, represent the diagnostic modes of the inorganic cage, being related to the bending and to the stretching modes of the *Pb−I* bonds, respectively. The peak at 119 cm^{-1} has been associated with the MA libration modes along with the unstructured feature in the frequency range of 150-160 cm^{-1}. Moreover, we found a broad, intense band at about 250 cm^{-1} assigned to the MA torsional mode [34, 35]. The latest, being sensitive to the specific organic-inorganic interactions (mainly occurring through Coulomb and hydrogen-bonds interactions between the NH_3 groups of the MA and the electronegative iodine atoms) represents an important marker of the orientational disorder of the material [34, 35]. In particular, in the more disordered phase of

$MAPbI_3$ (whose extreme is represented by the *cubic phase* for T>327 K [11]) the MA cations arrange in a random orientation within the inorganic cage due to their large orientational mobility [35]. This leads to a broadening and a red-shifting of the band at around 250 cm^{-1} [35]. On the contrary, in the more ordered "head to tail" arrangement [34] of the MA cations (whose extreme is represented by the *orthorhombic phase* for T<160 K [11]), this band looses intensity (by symmetry selection rules) and it considerably blue-shifts [34]. Finally, the broad shoulder peaking at ~160 cm^{-1} has been previously assigned to libration of the MA cations, calculated at 156 cm^{-1}. From the simulation it also is expected to become sharper and more intense, in the more ordered "head to tail" arrangement [35].

Analyzing the evolution of the Raman spectrum from the "meso" to the "flat" $MaPbI_3$ sample (see Figure 1 and fitted single peaks as dot lines along with fitted parameters collected in Table SI) a clear trend is visible at a first glance: i) the broad band at around 250 cm^{-1} blue-shifts and its intensity strongly decreases; ii) the peak at 119 cm^{-1} decreases in intensity and red shifts (from 119 cm^{-1} to 115 cm^{-1}); iii) the broad band at around 160 cm^{-1} becomes sharper and more resolved, clearly peaking now at 163 cm^{-1}; iv) the peak at around 94 cm^{-1} gains strength.

According to the discussion above, these observations highlight the different organic-inorganic interactions affecting the orientational order of the organic cation in the unit cell when the perovskite film is grown on the two different substrates. The experimental findings point to a clear trend, that is, an ordered ("head-to-tail" like) arrangement [34, 35] of the MA cations in "flat" samples versus a more disordered cations arrangement in the "meso" sample, similar to the effect observed on the IR spectrum of $MAPbI_{3-x}Cl_x$ when decreasing the temperature [35].

It is also important to notice that as a consequence of increasing structural order, the peak at 94 cm^{-1} is also affected: it increases in intensity and gets sharper. Together with the reduction of the

close peak at 119 cm^{-1}, this appears in the spectra as an inversion of their relative amplitude. A similar effect has been already observed in literature when comparing pure ordered PbI_2 crystals (for which the mode at 96 cm^{-1} represents the main peak [36]) with ammonia-intercalated PbI_2 compounds, forming a "distorted" crystal, which shows the same, reversed relative intensity [36]. Thus, the intensity of the mode at 119 cm^{-1} is another marker of the local distortion. Overall, our analysis suggests that while crystallization of $MAPbI_3$ on "flat" substrates leads to large crystals with a rather ordered arrangement of the organic cation, crystallization within the constraints imposed by the "meso" metal-oxide scaffold leads to small crystals which retain a disordered configuration at the molecular level.

Although the MA cations do not directly participate to the frontier orbitals of the semiconductor [36] however, its interaction with the inorganic cage and the displacement of the organic cation may affect the electronic properties of the compound [38]. In agreement, we observe a red shift of the UV-VIS absorption onset when moving from "meso" to "flat" $MAPbI_3$ film (see Figure 1b). It must be also noted that some of us have experimentally observed a clear excitonic transition - already evident just below room temperature - at the onset of the "flat" $MAPbI_3$ absorption spectrum [19]. On the other hand, no excitonic transition has been observed, even at 4K, for the "meso" film. Notably, Even *et al.* [22] have recently modeled an excitonic transition with an exciton binding energy of only 5 meV and they assigned the small binding energy to exciton screening by collective motion of the MA cations. This suggests that the preferential order of the organic cation in the "flat" film may possibly slow down the rotational motion of the MA cations which may in turn affect the screening of the excitonic transition at the on-set of the absorption spectrum.

In Figure 2a we compare the normalized Raman spectra of the flat $MAPbI_3$ film with the one from the *Cl-doped* $MAPbI_3$ on a mesoporous Al_2O_3 scaffold. We observe that the Raman spectra of the "meso" *Cl-doped* $MAPbI_3$ resembles very much that of the "flat" $MAPbI_3$, keeping the same Raman peaks and relative intensity.

This result demonstrates that the presence of chloride ions in the starting composition does not change the chemical nature of the inorganic cage, but it affects the local structure, inducing a preferential order of the MA cation organization in the inorganic cage even in the mesostructured samples. To gather more information on the crystallization process of the *Cl-doped* $MAPbI_3$ we have monitored the chemical species formation during the film crystallization combining Raman spectroscopy with steady state photoluminescence (PL) spectroscopy. In particular, we have identified three critical steps during the perovskite film formation on a mesoporous alumina scaffold: step 1) deposition by spin coating of the precursors' solution with no further annealing; step 2) film annealed for 4 minutes at 100° C; step 3) film annealed for 45 minutes at 100° C. We prepared one sample for each step and we measured their relative Raman spectrum as shown in Figure 2b (see also Table SI in Supplementary Information for retrieved parameters). For comparison, also the Raman spectra of the $PbCl_2$ and MAI precursors are shown. The film fabricated up to step 1) exhibits a Raman spectrum showing a main broad peak at around 104 cm^{-1}, related to the *Pb-I* bending and stretching modes [36]. The spectrum loses the characteristic *Pb-Cl* features (see $PbCl_2$ spectrum in Figure 2.b), in line with the predicted thermodynamic stability of the $MAPbI_3$ perovskite upon Cl to I substitution [26] and suggests that despite the use of $PbCl_2$ precursor, *Pb-I* bonds are quickly formed. In accordance, the PL spectrum registered at step 1) peaks at 500 nm, confirming the presence of PbI_2 [30, 39] as primary species in the crystallization process before annealing (see Figure 1d). Upon 4 minutes annealing the Raman

spectrum dramatically changes: a main peak at 121 cm^{-1} appears along with a broad band peaking at 264 cm^{-1} (see Table I). As explained above, these features are the markers of the libration and torsional mode of the organic cation present within the inorganic cage, proper of the perovskite structure as previously discussed. Notably, it essentially resembles the Raman spectrum of the "meso" $MAPbI_3$ (see Figure 1a for comparison). This similarity indicates that this structure represents an intermediate phase in the *Cl-doped* perovskite film formation. In accordance, at step 2) the PbI_2 PL is not totally quenched, indicating that the perovskite conversion in not fully completed yet (Figure 2c). Finally, we measure the *Cl-doped* $MAPbI_3$ "meso" sample upon full conversion into the perovskite structure in step 3). The Raman spectrum of the "meso" *Cl-doped* $MAPbI_3$ is registered, as described before. This indicates that the longer annealing time in presence of the $PbCl_2$ precursor allows for a reorganization of the organic-inorganic moieties within the crystal. As expected, the PbI_2 PL is completely quenched and we only observe the emissive band peaking at 770 nm (Figure 2c), typical of the *Cl-doped* $MAPbI_3$ [30]. Our analysis suggests that the chloride ions in the *Cl-doped* $MAPbI_3$ are not present within the crystalline unit cell bounded to the lead atom, neither any $PbCl_2$ residual is left over, but Cl has an important role in governing the crystallization process and the arrangement of the organic moieties.

To get a further insight into the local crystalline arrangement, we performed XRD analysis of both $MAPbI_3$ and *Cl-doped* $MAPbI_3$ in "flat" and "meso" samples. Figure 3 shows the XRD experimental data (dotted curves) along with the Rietveld fitted profiles [40] (continuous curves) and the markers of the $MAPbI_3$ reference structure for all the investigated thin films. A summary of the refined parameters are reported in Table I. Figures 3a-d indicate that the XRD patterns were correctly indexed as the $MAPbI_3$ crystal structure majority phase. The retrieved parameters

clearly show that the presence of Cl in the precursors does not affect significantly the unit cell parameters, for whatever substrate, as it would have been expected for Cl ions entering as substitutional impurities in the lattice according to the Vegards's law [41, 42] (see "XRD data analysis" section of the Supplementary Information for details on XRD spectra analysis). We have also performed an analysis of the preferred orientations (POs) along the [004] and [220] crystallographic directions. In Table I we report the fitted March parameter (G1), $0 < G1 < 1$, which is an indicator of the strength of the preferred orientation along a selected preferential crystallographic direction: at $G_1 = 1$ (random powder) there is no orientation; at $G_1 = 0$ (perfect uniaxial preferred orientation), there is total preferred orientation. First of all, we can highlight a trend which depends on the nature of the substrate, i.e. crystals grown on the flat substrate present grains that are much more oriented with respect to the mesoporous substrates. In addition there is an evident effect related to the presence of Cl. For the flat substrate, the Cl doping induces slightly more pronounced and, strongly unbalanced orientation of the grains in the [220] crystallographic direction, i.e. 88% of the grains present G_{220} =0.2200, 12% of the grains G_{004}= =0.600. Notably these grains also reach the largest extension (about 1000 Å). In the case of the "meso" samples, the Cl doping increases the (220) PO degree - G_1 reduces from 0.4815 to 0.2542 going from $MAPbI_3$ to *Cl-doped* $MAPbI_3$. In this case it must be noted that a preferential interaction of chloride with the metal-oxide surface has been computationally predicted [43]. We have also extended this analysis to two further deposition procedures widely used to optimize the surface coverage in the device fabrication: "two steps" deposition of $MAPbI_3$ obtained from MAI and PbI_2 [3] and vapor deposition *Cl-doped* $MAPbI_3$ [6] obtained after co-evaporation of the $PbCl_2$ and MAI precursors on a flat substrate (see Supporting Information, Fig S3). While the "two steps" $MAPbI_3$ shows a large G1 factor for both the (004) and (220) POs, we find a

majority of (220) oriented grains in the vapor deposition *Cl-doped* $MAPbI_3$ on compact TiO_2 ($G1_{220}$=0.2800 The unit cell parameters of the evaporated *Cl-doped* perovskite film retrieved from the analysis are listed in Table I. In conclusion, no signature of Cl in the unit cell is present, in accordance with the Raman analysis, but its presence in the precursor solution strongly affects the mesoscopic structure of film.

As a final point we aim to understand if the Cl ions, even if absent in the unit cell, are still retained in the perovskite film. Thus, to visualize the presence of Cl atoms we performed Energy Dispersive X-ray spectroscopy (EDS) analysis on *Cl-doped* perovskite films deposited on the mesoporous Al_2O_3 and flat glass, or evaporated on a flat substrate. In Figure 4a (left panel) we compare the EDS compositional spectra from each sample in the [2, 3] keV energy region, typical for the main Pb and Cl lines, after normalization to the intensity of the Pb Mα line. A zoom into the range of Cl Kα lines (energies between 2.5 and 2.9 keV) is also reported (right panel) to emphasize the relevant differences we observed. It has to be noted that Cl Kα lines (usually centered at approx. 2.62 keV) slightly overlap with a minor Pb line (Pb Mγ, at 2.65 keV). In Figures 4b-d we show representative BSE-SEM images of the investigated samples ("flat", "evaporated" and "meso" respectively). For the "flat" and "evaporated" samples, though obtained from Cl-containing precursors, the observed chlorine content is always below the detection limit of the technique (0.1 wt. % in the analyzed volume), in agreement with what was recently reported by Docampo *et al.*, [32] on similar samples. Interestingly, a different scenario is found for the "meso" sample, where a Cl signal (approx. 0.2 wt. %, just above the detection limit) is detected. In order to gain a better insight, for the "meso" sample, we repeated the compositional analysis on different detection spots on a pure "meso" area (see green ellipse in Figure 4d), inside which nano-crystals of the hybrid perovskite have grown, and on a large

crystalline aggregate that constitutes the capping layer over the "meso" scaffold (red square in Figure 4.d). We find that the Cl signature is only detected from the pure "meso" areas where the capping layer is missing. In fact, the large crystallites grown on top of the scaffold do not show any detectable Cl signal (preliminary studies where the gas phase species evolution is monitored by means of a quadrupole mass spectrometer show evaporation of Cl during the annealing – data not shown). This suggests us that the metal-oxide scaffold plays a significant role in retaining the Cl ions.

In conclusion our investigations on $MAPbI_3$ and *Cl-doped* $MAPbI_3$ films highlight the complexity of these compounds and their extreme sensitivity to environmental stimuli. First of all, we have demonstrated that the simple choice of the substrate strongly affects the structural properties of the thin film from a molecular to a mesoscopic level. In particular we have clarified how the crystallization process influence the inorganic-organic moieties interplay and how this plays a role in determining the optical response of the thin film: leaving $MAPbI_3$ free to crystallize in larger crystals allows the organic cation to arrange itself in a head-to-tail-like configuration, with oriented grains. This results in a reduced strain on the *Pb-I* cage and in a reduced screening generated by the cation motion, thus affecting the nature of the electronic state at the optical absorption onset of the semiconductor. Raman and XRD analysis clearly points out that even in presence of Cl source in the crystallization process, *Pb-I* bonds are only found in the inorganic cage featuring the crystal unit cell. However, the presence of Cl can drive the crystallization dynamics, favoring a higher order of the organic moieties in the inorganic cage and inducing a preferred orientation of the crystalline grains even in small crystals, in contrast to $MAPbI_3$. Thus, the presence of Cl helps minimizing the morphological and energetic disorder of

the film, one of the main issue in the field of thin film solar cells. Importantly, the film made of small crystals grown within the mesoporous metal-oxide scaffold is found to retain small amount of Cl. This definitely opens new directions of studies in order to clarify whether the Cl has a role on the surface passivation of the crystal and how it affects the structural and electronic properties of the perovskite-metal oxide interface.

REFERENCES

1. Kojima, A.; Teshima, K.; Shirai, Y.; Miyasaka, T.; *J. Am. Chem. Soc.* **2009,** 131, 6050-6051.

2. Lee, M. M.; Teuscher, J.; Miyasaka, T.; Murakami, T. N.; Snaith, H. J., *Science* **2012**, 338, 643-647.

3. Kim, H-S.; Lee, C. R.; Im, J. H.; Lee, K. B.; Moehl, T.; Marchioro, A.; Moon, S. J.; Humphry-Baker, R.; Yum, J. H.; Moser, J. E.; Gratzel, M.; Park, N. G., *Sci. Rep.* **2012**, 2, 591-1-591-7.

4. Heo, J. H.; Im, S. H.; Noh, J. H.; Mandal, T. N.; Lim, C. S.; Chang, J. A.; Lee, Y. H.; Kim, H. J.; Sarkar, A.; Nazeeruddin, Md. K.; Gratzel, M.; Seok, S.I. *Nature Photonics* **2013**, 7, 486-491.

5. Burschka, J; Pellet, N.; Moon, S. J.; Humphry-Baker, R.; Gao, P.; Nazeeruddin, M. K.; Gratzel, M., *Nature* **2013**, 499, 316-319.

6. Liu, M.; Johnston, M. B.; Snaith, H. J. *Nature* **2013**, 501, 395-398.

7. Research Cell Efficiency Records, NREL, http://www.nrel.gov/ncpv/ accessed: June 2014.

8. Lee, J.V; Seol, D.J., Cho, A. N.; Park, N.G. *Adv. Mater.* **2014**, DOI: 10.1002/adma.201401137.

9. Jeon, N. J.; Lee, H. G.; Kim, Y. C.; Seo, J.; Noh, J.H.; Lee, J.; Seok S.I. *J. Am. Chem. Soc.* **2014**, 136 (22), 7837–7840.

10. Snaith, H. J. *J. Phys Chem. Lett.* **2013**, 4, 3623-3630.

11. Baikie, T.; Fang, Y.; Kadro, J. M.; Schreyer, M.; Wei, F.; Mhaisalkar, S. G.; Graetzel, M.; White, T. J. *J. Mater. Chem. A*. **2013**, 1, 5628-5641.

12. Zhao, Y., Zhu K., *J. Phys. Chem. C* **2014**, 118 (18), 9412–9418.

13. Stoumpos, C. C.; Malliakas, C. D.; Kanatzidis, M. G*., Inorg. Chem.* **2013**, 52, 9019-9038.

14. Eperon, G.E., Burlakov, V. M., Docampo, P., Goriely, A.; Snaith, H.J. *Adv. Funct. Mater.* **2014**, 24, 151.

15. Nanova, D.; Kast, A. K.; Pfannmöller, M.; Müller, C.; Veith, L.; Wacker, I.; Agari, M.; Hermes, W.; Erk, P.; Kowalsky, W.; Schröder, R. R.; Lovrinčić R.; *Nano Lett.* **2014**, 14 (5), 2735–2740.

16. Dualeh, A.; Tétreault, N.; Moehl, T.; Gao, P.; Nazeeruddin, M. K.; Grätzel, M. *Adv. Funct. Mater.* **2014**, 24, 21, 3250–3258.

17. Tan, KW.; Moore, DT.; Saliba, M.; Sai, H.; Estroff, LA.; Hanrath, T.; Snaith, H.J.; Wiesner, U.; *ACS nano* **2014**, 8 4730-4739.

18. Colella, S.; Mosconi, E.; Fedeli, P.; Listorti, A.; Gazza, F.; Orlandi, F.; Ferro, P.; Besagni, T.; Rizzo, A.; Calestani, G.; Gigli, G.; De Angelis, F.; Mosca, R. *Chem. Mater.* **2013**, 25, 4613-4618.

19. D'Innocenzo, V.; Grancini, G.; Alcocer, M. J. P.; Kandada, A. R. S.; Stranks, S. D.; Lee, M. M.; Lanzani, G.; Snaith, H. J.; Petrozza, A.; *Nat. Commun.* **2014**, 3586, doi:10.1038/ncomms4586

20. Hirasawa, M.; Ishihara, T.; Goto, T.; Uchida, K.; Miura, N.; *Physica B.* **1994**, 201, 427-430.

21. Ishihara, T.; *Journ. of Luminescence* **1994**, 60, 269-274.

22. Even, J.; Pedesseau, L.; Jancu, J.-M.; Katan, C.; *J. Phys. Chem. Lett.* **2013**, 4, 2999-3005.

23. Brivio, F.; Walker, A. B.; Walsh, A.; *Appl. Phys. Lett. Mat.* **2013**, 1, 042111-1-042111-5.

24. Filippetti, A.; Mattoni, A.; *Phys. Rev. B* **2014** 89, 125203.

25. Umari, P.; Mosconi, E.;De Angelis, F.; *Sci. Rep.* **2014**, 4, 4467.

26. Mosconi, E.; Amat, A.; Nazeeruddin, M. K.; Grätzel, M.; De Angelis, F.; *J. Phys. Chem. C* **2013**, 117 (27), 13902–13913

27. Ball, J.M.; Lee, M. M; Hey, A.; Snaith, H. J *Energy Environ. Sci.* **2013**,6, 1739-1743

28. Choi, J. J.; Yang, X.; Norman, Z. M.; Billinge, S. J. L.; Owen, J. S. *Nano Lett.* **2014**, 14 (1), 127–133.

29. Sum, T. C.; Mathews, N.; *Energy Environ. Sci.*, **2014**, DOI: 10.1039/C4EE00673A.

30. Stranks, S. D.; Eperon, G. E.; Grancini, G.; Menelaou, C.; Alcocer, M. J. P.; Leijtens, T.; Herz, L. M.; Petrozza, A.; Snaith, H. J. *Science* **2013**, 342, 341-344.

31. Xing, G; Mathews, N.; Sun, S.; Lim, S. S.; Lam, Y. M.; Gratzel, M.; Mhaisalkar, S.; Sum, T. C. *Science* **2013**, 342, 344-347.

32. Docampo, P.; Hanusch, F.; Stranks, S. D.; Döblinger, M.; Feckl, J. M.; Ehrensperger, M.; Minar, N. K.; Johnston, M. B.; Snaith, H. J.; Bein, T. *Adv. Energy Mater*. **2014**, DOI: 10.1002/aenm.201400355

33. Loi, M. A.; Hummelen, J. C. *Nature Mater.* **2013**, 12, 1087-1089.

34. Quarti, C.; Grancini, G.; Mosconi, E.; Bruno, P.; Ball, J. M.; Lee, M. M.; Snaith, H. J.; Petrozza, A.; De Angelis, F. *J. Phys. Chem. Lett.* **2014**, 5, 279−284.

35. E. Mosconi, C. Quarti, T. Ivanovska, G. Ruani and F. De Angelis, *Phys. Chem. Chem. Phys*., **2014**, DOI: 10.1039/C4CP00569D.

36. Preda N; Mihut, L.; Baibarac, M.; Husanu, M.; Bucur, C.; Baltog, I.; *J optoelectron adv m* **2008**, 10,2, 319-322.

37. Borriello, I.; Cantele, G.; Ninno, D.; *Phys. Rev. B* **2008**, 77, 235214.

38. Amat, A.; Mosconi, E.; Ronca, E.; Quarti, C.; Umari, P.; Nazeeruddin, M. K.; Grätzel, M.; De Angelis, F., *Nano Lett.* **2014**, 14 (6), 3608–3616.

39. Preda. N.; Preda, L.; Mihut, I.; Baltog, C.; Velula, T.; Teodorescu, V.; *J optoelectron adv m* **2006** 8, 3, 909-913.

40. Rietveld, H. M. *J Appl Crystallogr* **1969** 2 (2): 65–71.

41. Vegard, L. Zeitschrift für Physik **1921** 5 (1): 17–26.;

42. Denton, A. R.; Ashcroft, N. W. *Phys. Rev. A* **1991**, 43 (6); 3161–3164.

43. Mosconi, E.; Ronca, E.; De Angelis, F. *J. Phys. Chem. Lett.* **2014***, submitted*

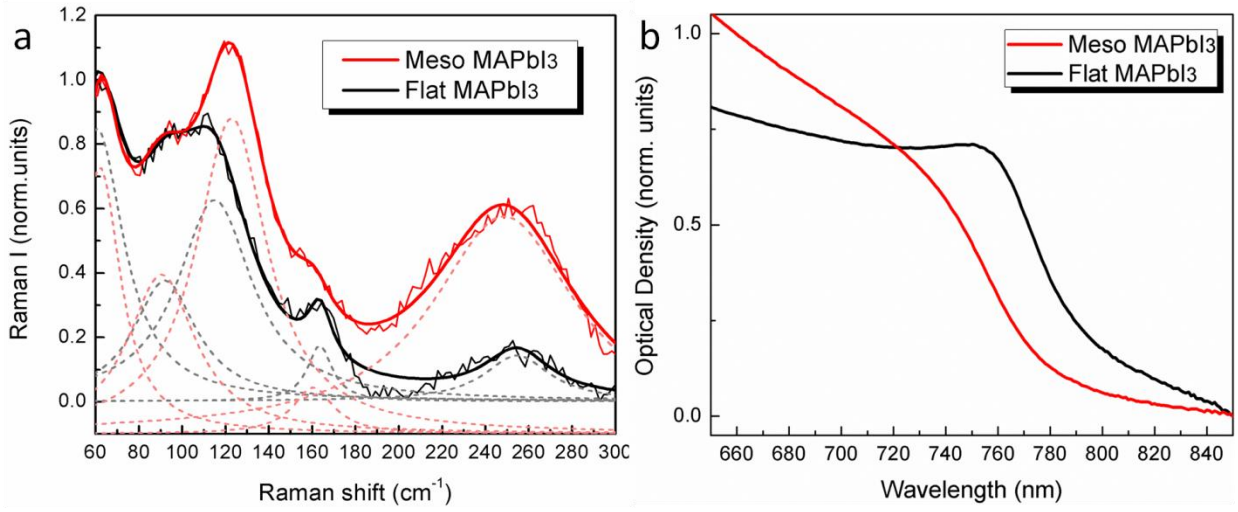

Figure 1 a. Resonant Raman spectra of "meso" MAPbI3 (red line) and of "flat" MAPbI3 (black line), see text for definition; dashed lines represent the Gaussian model used to fit the Raman peaks; the thick lines are the results of the fit, as the sum of the individual Gaussian functions. Excitation at 500 nm. **b.** Normalized optical absorption for the "meso" $MAPbI_3$ (red line) and the flat (black line) $MAPbI_3$ films.

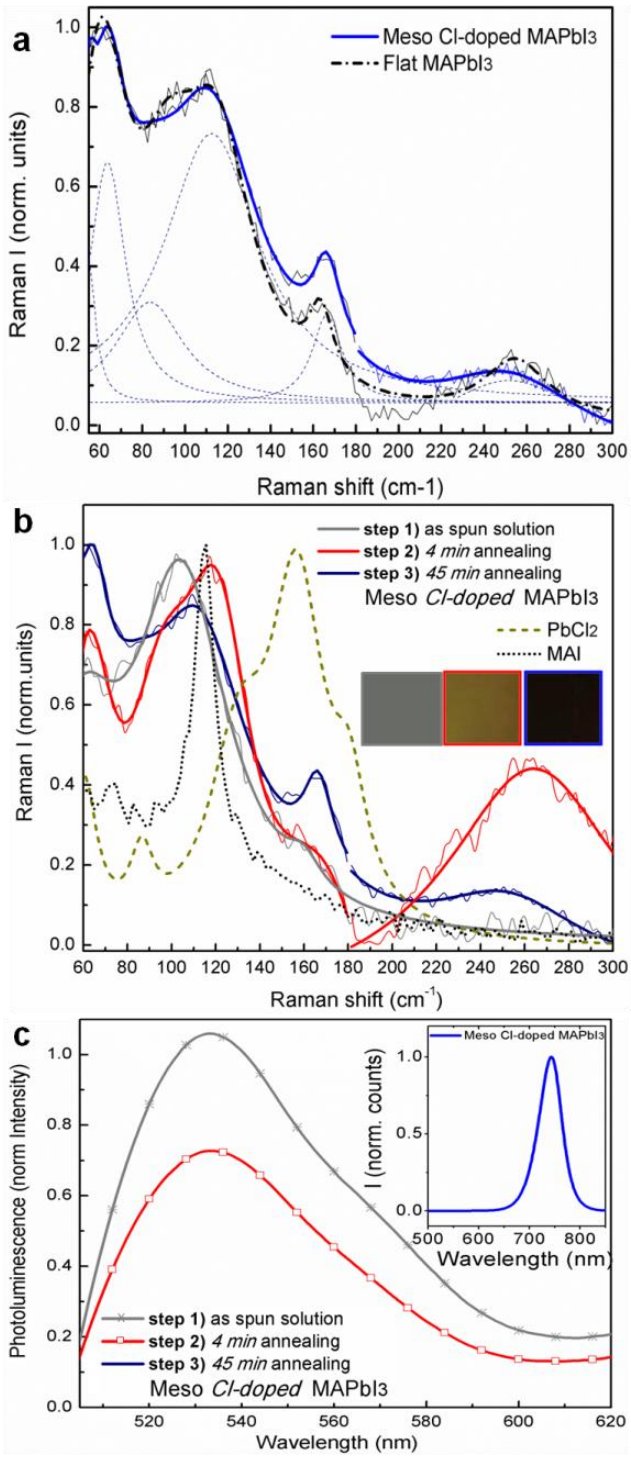

Figure 2 a. Resonant Raman spectra of Meso *Cl-doped* $MAPbI_3$ (blue line) and of flat $MAPbI_3$ (black dashed line); dotted line represent the Gaussian model used to fit the Raman peaks; thick line is the results of the fit, as the sum of the Gaussian curves. **b.** Raman Spectra of the

perovskite solution precursor and of the intermediate products during the *Cl-doped* $MAPbI_3$ film formation: step1) the "as spun" solution (grey line) as deposited on the substrate, step2) after 4 minutes annealing, and step 3) the final perovskite film obtained at the end of 45 minutes annealing. Inset: cartoon of the film evolution at the three steps mentioned. **c.** Photoluminescence spectra of the intermediate products during the *Cl-doped* $MAPbI_3$ film formation as for **b.** Excitation at 500 nm

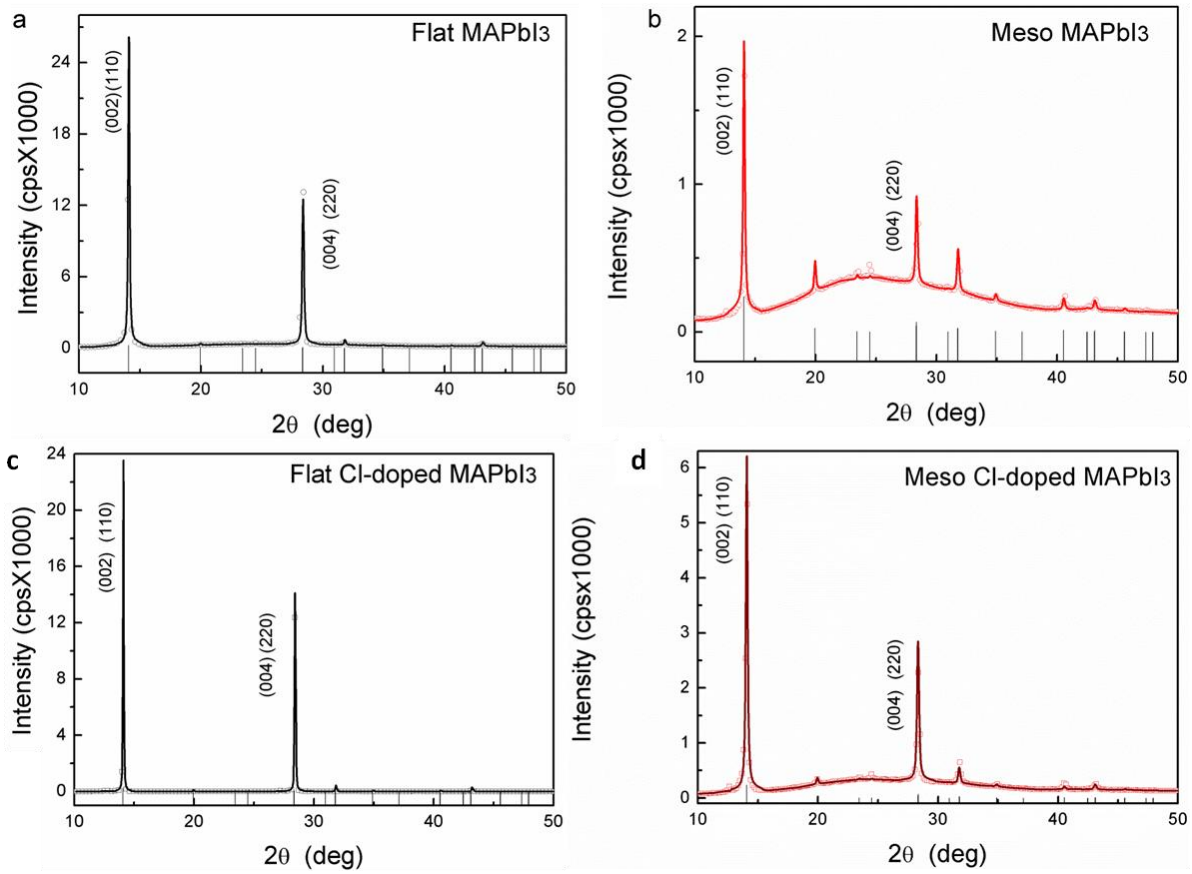

Figure 3 XRD analysis (experimental patterns and Rietveld fitted profiles) of $MAPbI_3$ (grown on "flat" – panel **a** – and on "meso" – panel **b** – substrates) and *Cl-doped* $MAPbI_3$ ("flat" – panel **c** – and "meso" – panel **d**) samples. The markers of the reference structure are reported as well.

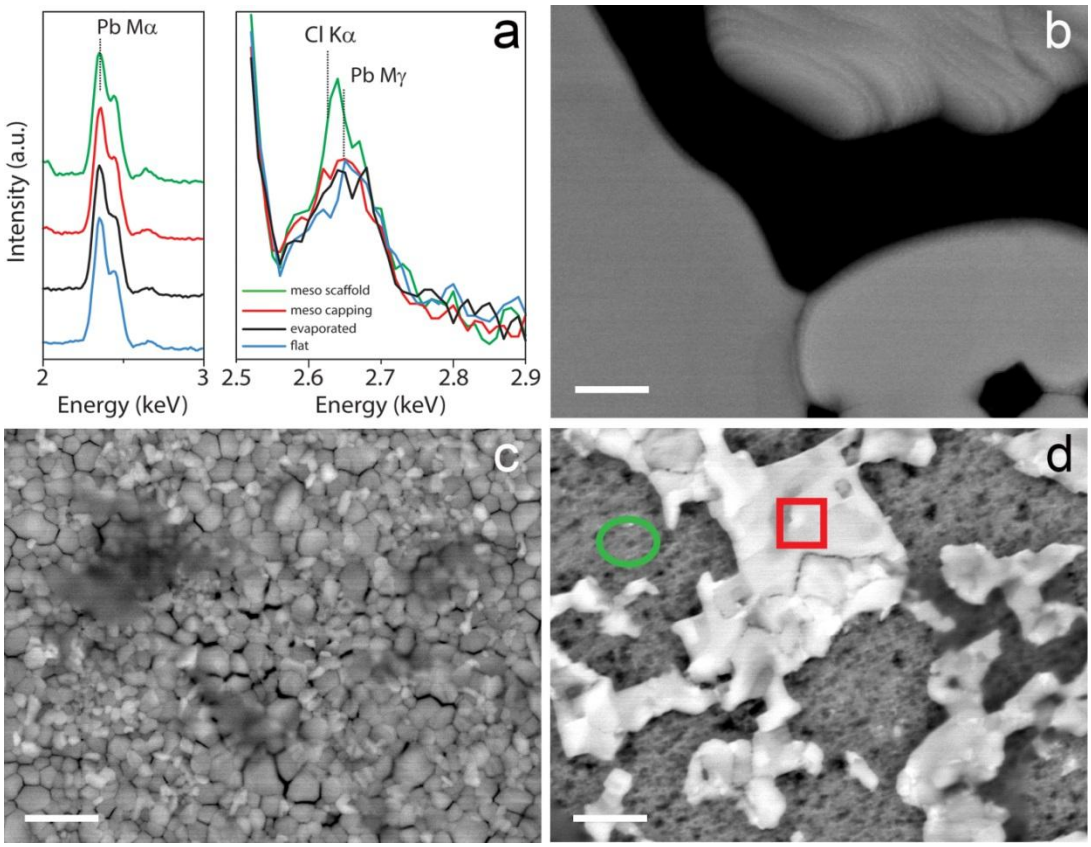

Figure 4 EDS elemental analysis (panel **a**) and representative BSE-SEM images (scale bar = 1 μm) collected on samples obtained from MAI and $PbCl_2$ precursors via spin coating on flat quartz substrate ("flat", panel **b**), evaporation on TiO_2 substrate ("evaporated", panel **c**) and spin coating on mesoporous Al_2O_3 scaffold ("meso", panel **d**). The EDS analysis is reported on the energy range typical for Pb and Cl main lines (see text for details). On the "meso" sample, EDS analysis was performed on areas of different morphology (that is, with or without the capping layer, see text for a more detailed description), as indicated by the green ellipse ("scaffold", no capping layer) and by the red square ("capping"). Cl signal was detected only on the "scaffold" regions of the "meso" sample.

Table I G1 (for different crystallographic directions, [220] and [004], togheter with the % of the oriented grains found in the film), a and c Parameters retrieved from XRD data fitting.

sample	$G1_{004}$ (%±5%) $G1_{220}$(%±5%)	a (Å)	c (Å)
Flat $MAPbI_3$	0.2253 (17%) 0.2550 (83%)	8.887	12.650 c/a=1.423
Flat *Cl-doped* $MAPbI_3$	0.6000 (12%) 0.2200 (88%)	8.877	12.650 c/a=1.423
Meso $MAPbI_3$	0.5019 (10%) 0.4815 (90%)	8.875	12.660 c/a=1.426
Meso *Cl-doped* $MAPbI_3$	0.7539 (25%) 0.2542 (75%)	8.890	12.641 c/a=1.422
Meso $MAPbI_3$ (2 steps)	0.7664 (16%) 0.6188 (84%)	8.875	12.673 c/a=1.428
Evap Flat *Cl-doped* $MAPbI_3$	0.6000 (22%) 0.2800 (78%)	8.880	12.641 c/a=1.423

Supporting Information. Experimental Methods, Tables including all the parameters and fit procedure for the Raman analysis and fitting details on XRD measurements are included in the Supporting Information. This material is available free of charge via the Internet at http://pubs.acs.org.

Corresponding Author

*mirko.prato@iit.it; *annamaria.petrozza@iit.it

Author Contributions

The manuscript was written through contributions of all authors. All authors have given approval to the final version of the manuscript. GG performed Raman Measurements; GE and MDB prepared the samples; SM and MP performed XRD and EDS measurements; CG performed the XRD fitting analysis; CQ and FDA calculated Raman modes; all the author analyze the data.

Funding Sources

Meso-superstructured Hybrid Solar Cells –MESO NMP-2013-SMALL7-604032.

Acknoledgments

The author thanks Dr Paola Bruno, Dr. A. Kandada and V. D'Innocenzo for valuable discussion, M. Gandini for the help in the sample preparation; E. Biserni for the help with Raman setup.